Journal of Nuclear Materials 385 (2009) 268–277

Contents lists available at ScienceDirect

Journal of Nuclear Materials

journal homepage: www.elsevier.com/locate/jnucmat

Numerical prediction of thermodynamic properties of iron–chromium alloys using semi-empirical cohesive models: The state of the art

G. Bonny [a,b], R.C. Pasianot [c,d], L. Malerba [a,*], A. Caro [e], P. Olsson [f], M.Yu. Lavrentiev [g]

[a] Nuclear Materials Science Institute, SCK CEN, Boeretang 200, 2400 Mol, Belgium
[b] Center for Molecular Modeling, Ghent University, Proeftuinstraat 86, B-9000 Gent, Belgium
[c] Departamento de Materiales, CAC-CNEA, Avda. Gral. Paz 1499, 1650 San Martín, Pcia. Buenos Aires, Argentina
[d] CONICET, Avda. Rivadavia 1917, 1033 Buenos Aires, Argentina
[e] Lawrence Livermore National Laboratory, Chemistry, Materials and Life Sciences Directorate, Livermore, CA 94550, USA
[f] Department Matériaux et Mécanique des Composants, Electricité de France, F-77250 Moret-Sur-Loing, France
[g] EURATOM/UKAEA Fusion Association, Culham Science Centre, Oxfordshire OX14 3DB, United Kingdom

ARTICLE INFO

PACS:
64.70.K–
64.70.kd

ABSTRACT

In this work the capability of existing cohesive models to predict the thermodynamic properties of Fe–Cr alloys are critically evaluated and compared. The two-band model and the concentration-dependent model, which are independently developed extensions of the embedded-atom method, are demonstrated to be equivalent and equally capable of reproducing the thermodynamic properties of Fe–Cr alloys. The existing potentials fitted with these formalisms are discussed and compared with an existing cluster expansion model. The phase diagram corresponding to these models is evaluated using different but complementary methods. The influence of mixing enthalpy, low-energy states and vibrational entropy on the phase diagram is examined for the different cohesive models.

1. Introduction

High-chromium ferritic/martensitic steels are candidate structural materials for advanced fission reactors, accelerator-driven systems using spallation neutron sources and fusion reactors [1]. One of the reasons for these steels to be selected as reactor core materials is their superior resistance to irradiation, in terms of low damage accumulation and low swelling, as compared to e.g. austenitic steels [2–5]. Nonetheless, in future nuclear systems it is expected that materials will be subjected during operation to very harsh irradiation and environmental conditions [1], not easy to withstand even for the best material choice. A quantitative understanding of the mechanisms leading to the change of the properties of these steels after long-term exposure to irradiation is therefore recognized to be of high importance for a safe design and operation of innovative nuclear systems [6]. A great deal of understanding can be achieved by studying simpler model systems such as, in this case, Fe–Cr alloys. For this reason, in recent years significant effort has been put for the development of numerical multi-scale models of the response to irradiation of these alloys (e.g. [7,8]). These models have the ambition of deducing the macroscopic response of the material to given conditions starting from a detailed knowledge of the fundamental interactions between atoms. It is a long-term approach that bears, however, the promise of being reliable, transferable and beyond empiricism.

The starting point for such an approach is a cohesive model for the description of the atomic interactions in the material of interest that should be applicable to millions of atoms, i.e. beyond the capabilities of *ab initio* methods, restricted to a few hundreds of atoms at the most. In the case of an alloy, a correct description of its thermodynamic properties, in terms of phase stability and equilibrium atomic distribution vs. temperature and concentration, may be seen as a necessary condition that such a cohesive model should fulfill, in order to be reliably used to model both equilibrium and out of equilibrium phenomena taking place under irradiation.

The Fe–Cr solid phase diagram, if the high temperature σ-phase region is neglected, is relatively simple, with only a large miscibility gap (MG) between two body-centred-cubic (bcc) phases, one rich in Fe, named α, the other rich in Cr, denoted as α'. Fig. 1 shows the standard Fe–Cr phase diagram, as built using the Calphad database [9] and essentially coincident with the phase diagram published in [10]. In this figure, the metastable MG, i.e. the MG that would exist if the σ-phase did not form, is also shown. Since the formation of the σ-phase is very slow under thermal ageing, its formation is in fact invariably preceded by α-α' phase separation [11–13]. Thus, for most purposes it is the metastable MG that counts to describe the thermodynamics of the system. Henceforth, this metastable MG is referred to as, simply, MG. From the figure, it

* Corresponding author. Tel.: +32 14 333090; fax: +32 14 321216.
E-mail address: lmalerba@sckcen.be (L. Malerba).

0022-3115/$ - see front matter © 2008 Elsevier B.V. All rights reserved.
doi:10.1016/j.jnucmat.2008.12.001

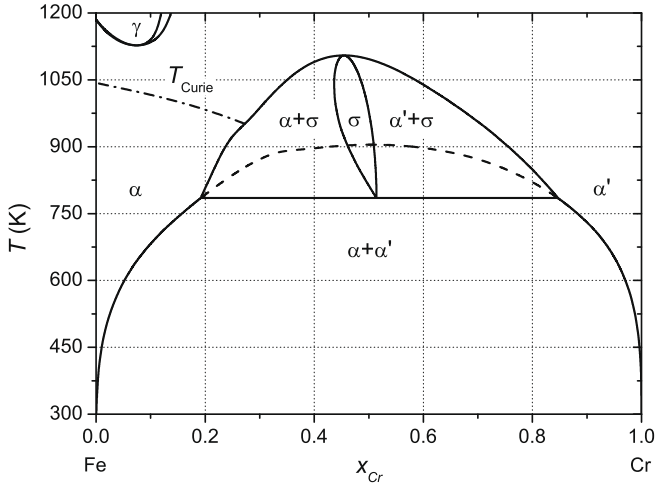

Fig. 1. Portion of the Fe–Cr solid phase diagram according to Calphad [9]. The dashed line indicates the metastable α–α' miscibility gap, and the dash-dotted line indicates the Curie temperature.

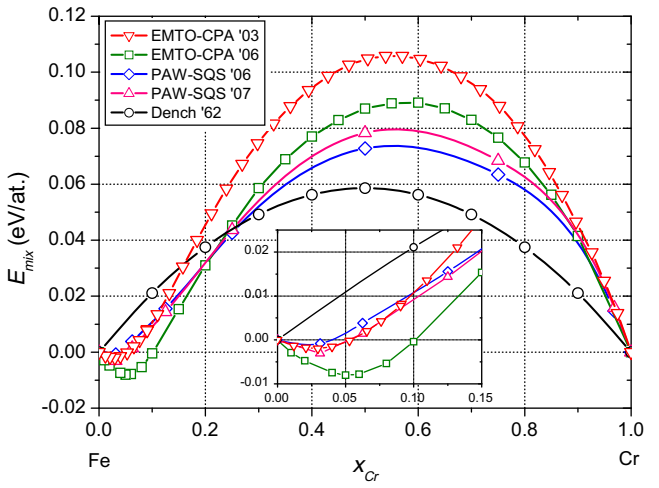

Fig. 2. The mixing enthalpy curves at 0 K for random or quasi-random ferromagnetic Fe–Cr alloys according to different DFT techniques [16,19,21], as discussed in the text. For comparison, the only existing experimental data, obtained for the paramagnetic phase [56], are also shown.

can be seen that, while the complete closure of the MG, including the σ-phase, occurs at about 1100 K, the metastable MG closes at about 900 K (for experimental data showing this, see Ref. [10]).

Notwithstanding its apparent simplicity, the microchemical behaviour of the Fe–Cr system is not trivial. Resistivity measurements and neutron scattering studies on well-annealed alloys revealed the existence, at about 700 K, of an inversion of the sign of the short-range order (SRO) parameter from negative (at 5% Cr) to positive (at 15% Cr), the zero crossing occurring at about 10% Cr [14]. This means that in Fe–5% Cr solute atoms tend to be surrounded by Fe atoms, while in Fe–15% Cr they tend to be surrounded by Cr atoms, i.e. to aggregate (giving rise to precipitation of the α'-phase). This effect has been confirmed by more recent Mössbauer and X-ray studies at different temperatures [15]. An explanation for the origin of this inversion of the sign of the SRO came recently from density functional theory (DFT) calculations. Different studies, performed with different DFT methods, showed that the mixing enthalpy of random, quasi-random and ordered ferromagnetic Fe–Cr solid solutions is negative below a critical concentration and becomes positive above it [16–22]. Data for random and quasi-random ferromagnetic alloys are shown in Fig. 2. Although quantitative differences exist between different DFT approximations (the critical concentration shifts between about 4% and 10% Cr and the depth of the negative well changes, too), the results are qualitatively similar and in clear agreement with the above mentioned experiments, as will be further shown in this work, since a negative mixing enthalpy implies conceptually that Cr atoms prefer to be surrounded by Fe, rather than by Cr atoms. The analysis of the DFT results provided also a clear physical explanation for this effect in terms of electron-band and magnetic properties of Fe and Cr [18,19]. The single Cr atom prefers to be surrounded by Fe atoms and Cr has, therefore, a negative heat of formation, as a consequence of a lowering of the density of states at the Fermi level, thus a lowering of the total energy, as extensively discussed in [19]. In addition, pure Fe is ferromagnetic in its ground state and pure Cr can be described as antiferromagnetic in its ground state [18,23]. However, a Cr atom surrounded by Fe atoms has an antiparallel magnetic moment to those of the Fe atoms [18,23]. If a second Cr atom is introduced nearby, the effect of 'magnetic frustration' occurs [18]. The latter is because either Cr atom favours its magnetic moment antiparallel to Fe as well as to Cr neighbours. When many Cr atoms are close to each other in Fe, different magnetic configurations can result from the competition [18]. In dilute alloys, the energetically most favourable situation is obtained when the Cr atoms are distributed sufficiently far from each other to avoid magnetic frustration (i.e. by ordering the alloy). When, however, the concentration of Cr is high enough, Cr–Cr interactions cannot be avoided, leading to a positive formation enthalpy, i.e. to a tendency to segregate. Additional insight has been obtained very recently, pointing out that the negative short-range order found for sufficiently low-Cr concentrations is not only the result of a pure repulsion between Cr atoms, but that, in addition, an effective long-range attractive interaction between Cr atoms exist, which appears to stabilise precise intermetallic phases, endowed with long-range order, at low temperature [22].

Reproducing this change of sign of mixing enthalpy and SRO parameter vs. concentration in Fe–Cr with a semi-empirical cohesive model has been in the last few years one of the main challenges for Fe–Cr modellers [7,8,24]. Doing this involves the introduction of an explicit or implicit dependence on concentration for the sign of the interactions. This task was soon realised [24,25] to be out of the scope of, for example, the traditional embedded-atom method (EAM) [26], or the functionally equivalent second-moment tight-binding approximation [27], calling for different formalisms to be developed. Given the largely magnetic origin of the afore described behaviour of Fe–Cr alloys, some recipe to include information about spins should *a priori* be considered and a simple example of such a model has been drafted in [28]. At the moment, however, no semi-empirical magnetic cohesive model for Fe–Cr has been fully developed and published to our best knowledge. Instead, three cohesive models exist, that do not explicitly include magnetism, but still reproduce the complex behaviour of Fe–Cr reasonably well. These models are: the cluster expansion (CE) developed by Lavrentiev et al. [29], the interatomic potential developed by Caro et al. [30] and the interatomic potential developed by Olsson et al. [31]. The latter two formalisms are *ad hoc* extensions of the standard EAM, where an additional term dependent on local concentration is introduced to reproduce the change of sign in the heat of mixing. In this work, the descriptions of the thermodynamic properties of Fe–Cr given by these three cohesive models, which represent the current state-of-the-art, are compared and critically discussed, with a view to determining their range of validity from the thermodynamic standpoint and to identifying which developments are still needed in order to come up with a fully reliable cohesive model for the Fe–Cr system

specifically, but also for any alloy in general. In particular, by separating effects in our analysis, we show that a number of 'ingredients' must be included in order to produce a cohesive model consistent with thermodynamics.

2. Semi-empirical cohesive models

CE techniques allow the energy (enthalpy) of an alloy to be expressed in terms of configurations of atoms on a (rigid) lattice with N sites, by using occupational spin variables, σ_i (one per lattice site), that, in the case of a binary alloy, take the values ±1 depending on whether the corresponding lattice site is occupied by one species or the other [32]

$$E(\vec{\sigma}_i) = J_0 + \sum_{\gamma} D_\gamma J_\gamma \prod_{i\in\gamma} \sigma_i. \tag{1}$$

Here $\vec{\sigma}_i = \{\sigma_i\}_{i=1,\ldots,N}$, J_0 is a constant, γ denotes any cluster defined on the lattice (lattice subset), J_γ are the effective cluster interactions (ECIs), i.e. the coefficients of the expansion to be fitted, and D_γ are the degeneracy factors (number of equivalent clusters in terms of symmetry). A smart choice of the clusters included in the expansion allows, by fitting the ECIs, the energy (enthalpy) for any lattice configuration to be properly reproduced. The result, however, is not directly sensitive to the displacements from the perfect lattice sites that atoms may experience due to strain field (relaxation) or temperature (vibration) effects. In order for these effects to be fully allowed for, interatomic potentials are needed, which, in the case of metals, are typically constructed in the EAM formalism. In this formalism, the total energy of a system of N atoms, whose type can be different and is denoted by t_i, can be written as

$$E = \sum_i \left[F_{t_i}\left(\sum_{j\neq i} \varphi_{t_i t_j}(R_{ij}) \right) + \frac{1}{2} \sum_{j\neq i} V_{t_i t_j}(R_{ij}) \right], \tag{2}$$

where F is the so-called embedding function, a functional of pairwise functions of the interatomic distances, each representing the electronic density contribution due to the surrounding atoms on the central one, and V is the pairwise energy contribution. Two modifications of this formalism have been proposed to fit a sign-changing mixing enthalpy, both focused on the proper fitting of the cross Fe–Cr interaction only, and otherwise using for the pure elements already existing potentials. In both cases the same pure element potentials have been adopted, namely the EAM-type Fe–Fe potential by Ackland et al. [33], developed using the methodology proposed and applied already in [34], and a second-moment tight-binding approximation Cr–Cr potential developed by Wallenius et al. [24]; both are state-of-the-art interatomic potentials for these two elements.

In the first modification [30], after renormalising the potentials for the pure elements in 'effective gauge' [27], an explicit dependence on concentration is introduced by multiplying the pair interaction term times a function $h_{t_i t_j}(x_{ij})$

$$E = \sum_i \left[F_{t_i}\left(\sum_{j\neq i} \varphi_{t_i t_j}(R_{ij}) \right) + \frac{1}{2} \sum_{j\neq i} h_{t_i t_j}(x_{ij}) V_{t_i t_j}(R_{ij}) \right], \tag{3}$$

with $h_{AA}(x_{ij}) = h_{BB}(x_{ij}) = 1$. Here x_{ij} represents the local concentration, which is postulated to be given by the average at the two interacting atoms of the ratio between partial and total electronic densities

$$x_{ij} = \frac{1}{2}\left(\frac{\rho_i^B}{\rho_i^{\mathrm{tot}}} + \frac{\rho_j^B}{\rho_j^{\mathrm{tot}}} \right), \tag{4}$$

where ρ_i^B represents the contribution to the electronic density on atom i coming from atoms of type B only, while ρ_i^{tot} is the total electronic density. The function $h_{t_i t_j}(x_{ij})$ can be written in the form of a typical Redlich–Kister expansion for thermodynamic functions (Calphad methodology) [9,35], with parameters fitted to closely reproduce the given reference mixing enthalpy curve and enables in principle any concentration dependence of such a curve to be recreated. This approach is henceforth denoted as *concentration-dependent method* (CDM).

The other modification [31] introduces the dependence on concentration in an indirect way and follows a somehow opposite route, by working on the embedding part, rather than on the pairwise potential. Namely, after drawing the attention on the fact that not only *d*-band electrons, but also *s*-band electrons participate in defining the energy of a transition metal alloy [31,36], Olsson et al. introduce two separate embedding functions, one for each band, as well as correspondingly separate electron density functions

$$E = \sum_i \left[F_{t_i}^d\left(\sum_{j\neq i} \varphi_{t_i t_j}^d(R_{ij}) \right) + F_{t_i}^s\left(\sum_{j\neq i} \varphi_{t_i t_j}^s(R_{ij}) \right) + \frac{1}{2} \sum_{j\neq i} V_{t_i t_j}(R_{ij}) \right]. \tag{5}$$

The concentration dependence is here contained in the *s*-band mixed electronic density (no *s*-band contribution is assumed in the case of the pure elements) and in practice the presence of the second embedding function provides sufficient degrees of freedom to fit closely any reference mixing enthalpy curve, as in the CDM case. This approach is henceforth denoted, for obvious reasons, as the *two-band method* (2BM).

Despite the apparent difference between the CDM (Eqs. (3) and (4)) and the 2BM (Eq. (5)) formalisms, it can be demonstrated that they are, in fact, very similar, as sketched in Appendix A.

3. Methodology for the evaluation of thermodynamic properties

3.1. Phase diagram computation

To obtain the phase diagram for each of the above-described cohesive models, three different, but complementary, methods were used.

The first and most naïve method involves the use of the regular solution model (RSM) [37], meaning that all the atoms are randomly distributed and that the only entropic contribution is configurational. This approximation is meaningful in the high temperature limit, because it neglects all configurational effects driven by low-energy ordered structures. At the same time, however, vibrational effects, which may become important at high temperature, are neglected and the enthalpy is assumed to be independent of temperature (its 0 K shape is maintained unaltered for the evaluation of the free energy at each temperature). Using this scheme, the mixing free energy per atom is easily expressed as

$$F(x,T) = E(x) - xE_{\mathrm{Cr}} - (1-x)E_{\mathrm{Fe}} + k_B T[x\ln(x) + (1-x)\ln(1-x)], \tag{6}$$

where E_{Fe} and E_{Cr} denote the cohesive energy of Fe and Cr, respectively, at 0 K. Using this free energy expression, the phase diagram is easily obtained by means of the common tangent method [37].

The second method consists of using the freely available ATAT package [38,39], which has been interfaced to an in-house molecular dynamics (MDs) code that works as 'energy engine'. Broadly, the package works in two stages: firstly, an automated statistically optimised procedure is followed in order to build a cluster expansion of the energy (this is where the MD code and the interatomic potential, enters; clearly, in the case of the CE model from [29] this step is skipped); secondly, the previous expansion is fed to a Monte Carlo code working in the transmutation (semi-grand canonical) ensemble for tracking the phase boundaries. The cluster expansion

is here used as an economic way to compute the energy of any configuration of the simulation box. The transmutation ensemble allows the species to change their nature, so that the controlling variables are temperature T and chemical potentials differences. The bcc simulation box referred to above is not strictly rigid, because atomic relaxations are accounted for when building the cluster expansion. This method takes the configurational entropy implicitly into account, making the effects of possible low-energy structures visible on the phase boundaries. The main shortcoming of such an approach is the lack of vibrational entropy, not explicitly included in the method.

Finally, the third method consists in complementing the first and/or second one by taking the vibrational entropy into account. For this purpose, two routes can be followed. One way is by introducing temperature dependent ECIs into ATAT, here pursued in the case of the 2BM potential. The pre-requisite for this route is a previous knowledge of the vibrational entropy implicit in the used cohesive model (this is possible for interatomic potentials; in the case of the CE from [29], the best that can be done is to estimate such a contribution over the whole range of compositions from available experimental data). Vibrational entropy calculations with interatomic potentials were therefore performed as described in Section 3.2. The other route involves applying a full thermodynamic integration for different alloy compositions [40], by exploiting MD techniques, thereby implicitly taking the vibrational entropy into account. The computational samples for the different concentrations can be produced in such a way that short-range order is explicitly accounted for, as shown in [41]. This method, however, can hardly take into account the possible existence and stability, according to the used cohesive model, of low-energy structures that may enter and modify the phase diagram built for random or partially ordered phases only. The stability of these structures for a given cohesive model is best obtained via a separate evaluation, as described in Section 3.3.

3.2. Vibrational entropy

Within the classical high temperature limit, the vibrational free energy of a system of oscillators, F_{vibr}, is expressed through the Debye temperature, T_D, according to [42]

$$F_{\text{vibr}}(T) = 3k_BT\ln(T_D/T), \tag{7}$$

neglecting optical modes and peculiarities of the phonon spectra. By applying the above to a binary alloy of solute concentration x, the vibrational free energy of formation (or excess vibrational free energy) is obtained as

$$F^{\text{mix}}_{\text{vibr}}(x,T) = 3k_BT\ln\left(\frac{T_D(x)}{(T_D^{\text{Cr}})^x(T_D^{\text{Fe}})^{1-x}}\right). \tag{8}$$

Note that, due to cancellation of kinetic energy terms, the above equation is nothing but the vibrational entropy contribution upon mixing, $-TS_{\text{vibr}}$. The goal is then to compute $T_D(x)$, for the purpose of which two approaches were followed; the first purely harmonic in nature, the second one incorporating some of the lattice anharmonicity.

The first approach (here termed MJS) gives an approximate formula for T_D based on full phonon spectra calculations for a number of cubic metals [43]

$$T_D = 0.617(6\pi^2)^{1/3}\frac{\hbar}{k_B}\left(\frac{\Omega^{1/3}B}{M}\right)^{1/2}, \tag{9}$$

where Ω denotes the atomic volume, M is the average mass and B is the bulk modulus of the alloy. To compute B, cubic boxes containing 2000 randomly distributed atoms were used.

The second approach involves MD runs on the above boxes for several temperatures relevant to the phase diagram. The samples were thermalised for about 20 ps and data on the mean squared displacements, $< r^2 >$, collected during the following 60 ps. Assuming the solid behaves as an average oscillator with Einstein-like frequency ω_E, energy equipartition leads to

$$\omega_E^2 = \frac{k_BT}{< r^2 > M}, \tag{10}$$

from which the Einstein temperature is easily obtained as $T_E = \hbar\omega_E/k_B$. It is clear that this allows for some temperature dependence in ω_E, that is carried over to $T_E(T_D)$, so that the approach may be termed 'quasi-harmonic' and is probably more accurate than the first, fully harmonic approach.

3.3. Possible ground states and low-energy states

For a binary alloy with a given lattice symmetry, there exist $\sum_{n=1}^{M}2^n$ possible ordered structures for a given unit cell containing up to M atoms. Whether wanted or not, a semi-empirical cohesive model may stabilise some of these structures. If so, it is important to know which ones, as in reality they may or may not exist and their presence influences the phase diagram as predicted by the cohesive model. These ordered structures can easily be enumerated as described in [44], but it is clear that the total number of structures increases fast with M, from which only a selected few represent possible ground states or low-energy states of the system of interest. It is thus desirable to sample these low-energy states instead of evaluating all possible ordered structures. A way to select ground states is based on the configuration polyhedron [45,46]. In short, given a lattice and a (set of) maximal cluster upon it, the configuration polyhedron is a convex region in the correlation functions (CFs) space where the probability of any specified cluster configuration is assured to be non-negative. The vertices of such a polyhedron are candidates to the system's ground states, though not all of the associated ordered structures are feasible, i.e. physically possible for the given lattice. In what follows we understand this concept in the latter more restricted sense of feasible vertices only. Also, here we denote the m-th CF for a cluster of n nodes as $\xi_{n,m}$.

Finel [47] studied the bcc lattice by using two maximal clusters, the standard octahedron and the cubic unit cell, so distances up to 5th nearest neighbour (5nn) were considered, except 4nn. From that work a polyhedron of 28 vertices (with 97 faces in the 5-D space of ξ_1, $\xi_{2,1}$, $\xi_{2,2}$, $\xi_{2,3}$ and $\xi_{2,5}$ coordinates) was constructed and the vertices were identified with the associated ordered structures. New vertices were then added by selecting ordered structures from previous ATAT runs, used to construct the bcc Fe–Cu phase diagram [48]. For each of these structures the respective CFs were determined in 6-D space using the point correlation function ξ_1 and five doublets up to 5nn: $\xi_{2,1}$, $\xi_{2,2}$, $\xi_{2,3}$, $\xi_{2,4}$ and $\xi_{2,5}$. Then these CFs were checked against the 28 original vertices given by Finel, with the result that the number of vertices of the polyhedron was raised up to 99 (with 1750 faces in 6-D space). The ordered structures corresponding to these vertices are referred to as BCC-99 and serve to sample possible ground states.

4. Results and discussion

4.1. The effect of the mixing enthalpy at 0 K on the phase diagram

As mentioned in the introduction, mixing enthalpy data for Fe–Cr alloys from different DFT calculations exist [16–22] and some of them have been used to fit the semi-empirical cohesive models analysed in this work. All available data for random and quasi-

random ferromagnetic mixtures are shown in Fig. 2, as calculated in the generalised gradient approximation (GGA) with spin polarisation, using two different methods: (i) a basis set of exact muffin-tin orbitals (EMTO), in the coherent potential approximation (CPA) to reproduce a fully random environment [16,19]; (ii) in supercells – with the projector augmented wave (PAW) method [49], as implemented in the VASP code [50–53] – where special quasi-random structures (SQS) [54] where created [19,21]. In the latter case, the difference between the two curves depends on whether the Vosko–Wilk–Nusair (VWN) interpolation of the correlation energy [55] is used [21] or not [19] (the complete set of data including this interpolation is here published for the first time). In the former case (EMTO–CPA calculations), the origin of the difference between the curves obtained in [16] and [19] for the ferromagnetic alloy would need to be investigated, but are likely due to the slightly different conditions used, which influenced the effective volume and, therefore, the mixing. As already remarked, the quantitative differences depending on the used method, even remaining within a DFT–GGA scheme, are non-negligible. EMTO–CPA-'03 provides a minimum comparable to the minimum predicted by PAW–SQS, although a much higher maximum. EMTO–CPA-'06 provides a significantly deeper minimum and again a higher maximum compared to PAW–SQS. The latest corrected PAW–SQS calculations, with the VNW interpolation, provide a curve that lays in-between the previous calculations and is accepted to be the most reliable. For reasons of comparison, also the experimental paramagnetic mixing enthalpy curve obtained at 1600 K [56], which is perfectly reproduced by non-spin-polarised EMTO–CPA calculations [16,19], is presented in the figure. The EMTO–CPA-'03 curve was used as reference to fit the CDM potential [30], while the PAW–SQS curve, without VWN interpolation, in its part for $x_{Cr} < 50\%$, was used as reference to fit the 2BM potential [31]. Concerning the CE from [29], the fitting was done on data for ordered structures, published in [18,20].

The mixing enthalpy curves calculated from the three cohesive models are presented in Fig. 3 and compared with, on the one hand, the Calphad curve [9,10], as extrapolated to 0 K from the corresponding Redlich–Kister expansion [35], and, on the other, the most recent PAW–SQS mixing enthalpy curve from Fig. 2. It can be observed that in no case is the fit of the potentials totally accurate. The CDM curve is indeed close to, although with a somewhat higher minimum and a somewhat lower maximum than, the EMTO–CPA-'03 curve, used as a reference for the fit. In addition, the CDM curve is fortuitously very close to the curve obtained from the CE from [29]. Conversely, the 2BM curve matches relatively well the PAW–SQS curve up to about 25% Cr, but, in the Fe-rich region, the values are more negative and closer to those of the EMTO–CPA curve. Above ~25% Cr, the 2BM curve lies clearly below the PAW–SQS curve and, fortuitously, approaches the Calphad curve which, in turn, is extremely similar to the experimental paramagnetic one, shown in Fig. 2. Finally, on the Cr-rich side, the 2BM curve presents a second negative region, thereby appearing symmetric. This symmetric shape, with negative regions on both sides, which is in disagreement with both the DFT ferromagnetic and the experimental paramagnetic data, corresponds to a deliberate choice made in [31], so that the fitting of the latter potential was in fact mixed: partly to DFT data and partly to other considerations (discussed later on). The implications for the phase diagram of the specific concentration dependence of the random alloy mixing enthalpy curves at 0 K according to the three different models are discussed in the following.

The phase diagrams obtained from the cohesive models within the RSM approximation are presented in Fig. 4. The MG closes at 3376, 2728 and 2652 K for CE, CDM and 2BM, respectively. These values, although inaccurate, represent an upper limit for the given model, since the randomly disordered alloy represents the high temperature limit. A first correlation between the mixing enthalpy curves and the phase diagrams can be found in the large solubility at low temperature in the Fe-rich region (~5% Cr at 300 K), which is an obvious consequence of the negative heat of mixing in that region for the three cohesive models. The large solubility at low temperature in the Cr-rich region for the 2BM is correspondingly also due to the negative heat of mixing on that side. It therefore appears that the choice of a symmetric mixing enthalpy curve makes the 2BM predict the concentration of Fe in the α'-phase to be non-negligible (~10% Fe), at temperatures of technological interest (<850 K), in agreement with experimental observations [12,13,57–59] (see also Ref. [60]), while CDM and CE yield essentially pure Cr precipitates. Despite this apparently 'good' result of the 2BM, deliberately imposing a negative heat of solution also for Fe in Cr to obtain this effect is probably not fully justifiable. Although experimentally, to our best knowledge, there are no data either proving or disproving this assumption, DFT calculations certainly do not support it. At the same time, though, DFT methods are known to fail to correctly

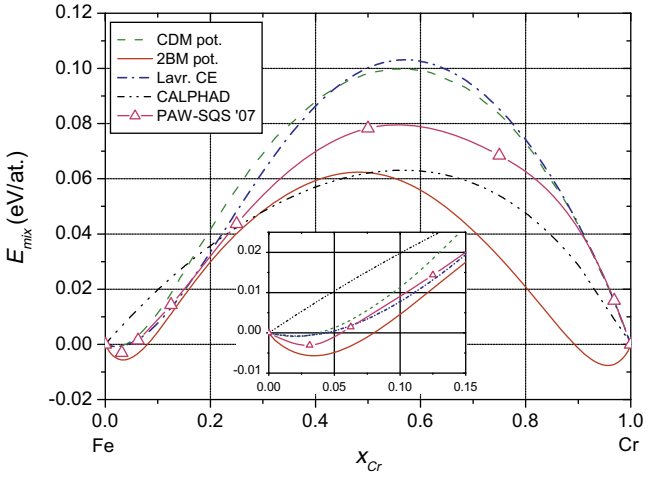

Fig. 3. Mixing enthalpy at 0 K for the Fe–Cr system according to CDM and 2BM potentials, as well as CE, in the random solution limit, compared with the most recent PAW–SQS data and with the Calphad curve (extrapolated to 0 K from the corresponding free energy expansion). The blow-up shows more in detail the sign-changing curves in the low-Cr region.

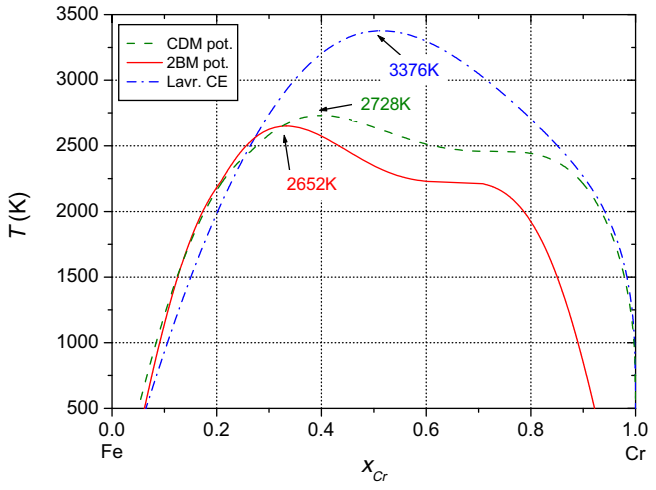

Fig. 4. The phase diagram according to the three cohesive models in RSM approximation.

predict the ground state for Cr [61,62], thereby suggesting caution concerning their full reliability in the Cr-rich region. Nonetheless, since a sign-changing mixing enthalpy should be considered an anomaly, in the absence of experimental evidence it would seem safer, so long as possible, to assume normal segregation, with positive heat of solution, to occur. However, at the moment semi-empirical cohesive models for Fe–Cr exhibiting positive mixing enthalpy in the Cr-rich region, while providing the correct α'-phase composition, have still to be produced and validated.

Turning now the attention to the shape and critical temperature for closure, T_{Crit}, of the MG, it is clear that there is no immediate obvious correlation with the mixing enthalpy curve. In particular, even though the mixing enthalpy curves from CDM and CE are similar, T_{Crit} differs by as much as 648 K. Moreover, the shape of the MG between CDM and CE appears to be completely different, the latter being the most symmetric. On the other hand, somehow surprisingly, the MG produced by 2BM and CDM appear to be very similar in shape and close at about the same T_{Crit} (the difference is only 76 K), while the difference in height between the respective mixing enthalpy curves is more than 37 meV. This comparison illustrates the inadequacy of a common misconception, according to which the height of the mixing enthalpy determines the closure temperature of the MG. A simple analysis shows that, more important than the height of the mixing enthalpy curve, is its curvature, which rationalizes the shape and T_{Crit} of the MG. It is easy to realise that the MG closes at the temperature where the second derivative (with respect to concentration) of the free energy becomes positive for all concentrations. Given the second derivative of the free energy, within the RSM approximation, as

$$F''(x,T) = E''_{\mathrm{mix}}(x) + \frac{k_B T}{x(1-x)}, \tag{11}$$

the critical temperature and concentration are given as the highest temperature for which $F'(x,T)$ can be zero. In Fig. 5, the corresponding expression for T_{Crit}, $T_{\mathrm{Crit}} = -\frac{x(1-x)}{k_B}E''_{\mathrm{mix}}(x)$, is plotted as a function of concentration for the three cohesive models. From this plot T_{Crit} and its composition are predicted. Even better, the curves clearly predict the shape of the MG (at high temperature), showing the importance of the curvature rather than the height of the mixing enthalpy.

To conclude this part, we show that all three semi-empirical models considered here, while not explicitly including spins, do manage to catch, if only from a purely phenomenological point of view, the effect of magnetism, in terms of not only the change of the sign of the mixing enthalpy, as shown, but also inversion of the SRO parameter. The driving force for this inversion is the Cr–Cr pair repulsion, which is the main consequence of magnetic frustration [18]. Fig. 6 shows that this repulsion is qualitatively, and largely also quantitatively, captured by all three models, with only minor and subtle differences, when compared to DFT values from Refs. [18,21]. It is noteworthy that none of these DFT repulsion energy values were used as fitting parameters for either potential. MC simulations aimed at reproducing the experimental results of Mirebeau et al. on the sign-change of the short-range order parameter [14] have also been performed with all three models. The results are shown in Fig. 7. It can be seen that all three cohesive models succeed in reproducing in a qualitatively correct

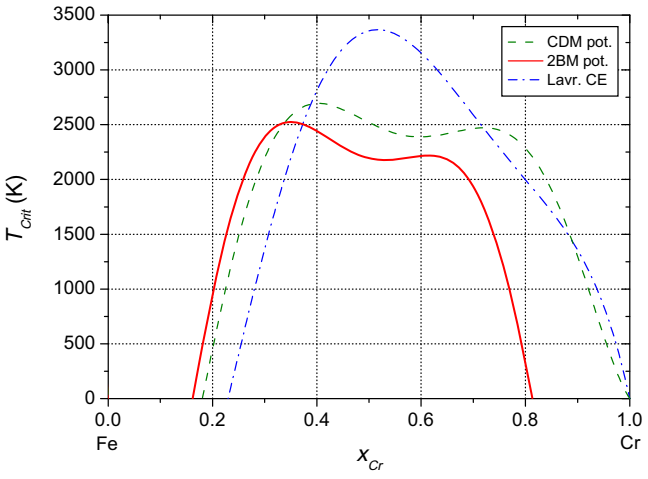

Fig. 5. The function $T_{\mathrm{Crit}} = -\frac{x(1-x)}{k_B}E''_{\mathrm{mix}}(x)$ for the three cohesive models.

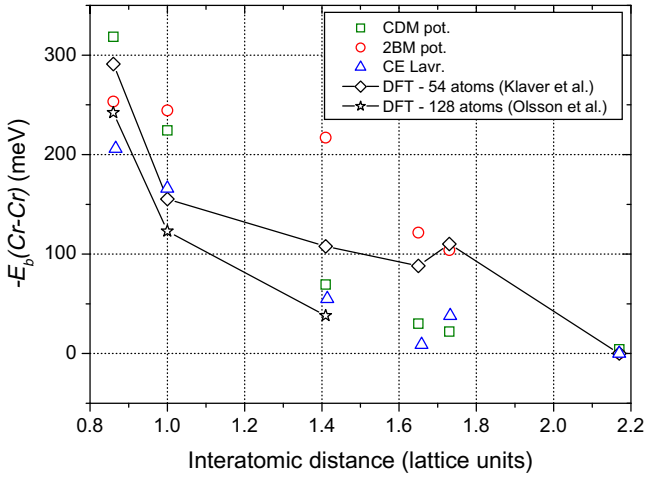

Fig. 6. Cr–Cr pair repulsive energy according to CDM and 2BM potentials, as well as CE, as compared with DFT data from [18] (54 atoms) and [21] (128 atoms) (The two sets of DFT data were obtained with the same code and approximation, so the difference is fully ascribable to box size effects). The values obtained with the potentials correspond to a fully converged box size.

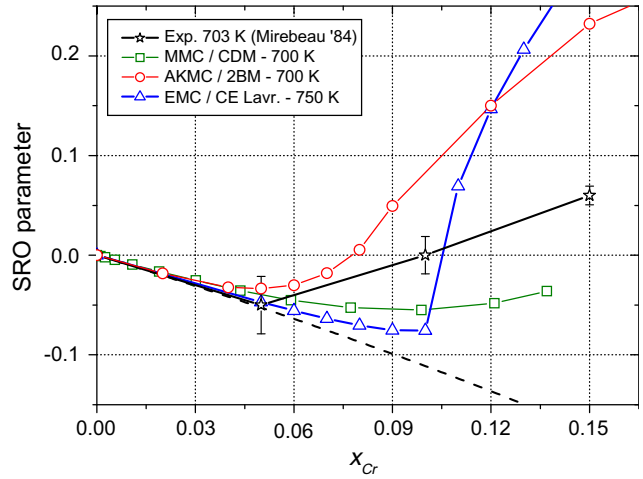

Fig. 7. Short-range order (SRO) parameter vs. Cr concentration according to simulations performed: (a) using a Metropolis MC method including relaxation with the CDM potential at 700 K [64]; (b) using an atomistic KMC method on rigid lattice with the 2BM potential at 700 K [63]; and (c) using an exchange MC method with the CE [29]. Also given, for comparison, are the corresponding experimental values from [14], as well as the limiting line (dashed), representing the minimum SRO parameter value theoretically possible.

way the experimentally observed SRO inversion in the low-Cr concentration range of Fe–Cr alloys, with some quantitative discrepancies from one model to the other, which are likely to depend also on the different modelling tools used for the simulation: atomistic kinetic Monte Carlo (AKMC) on rigid lattice with 2BM [60,63]; Metropolis Monte Carlo (MMC) in the transmutation ensemble including atomic relaxation with CDM [64]; exchange Monte Carlo (EMC) on rigid lattice in the case of the CE [29]. The main discrepancies between models and with respect to the experimental data concern the minimum SRO value reached, the extension of the region where the SRO is negative and the abruptness or smoothness of the transition to a positive value. In addition, the two models for which the study was extended beyond the point where phase separation occurred, predict a very positive SRO parameter after the sign-inversion, when compared to the experiment. This is a clear sign of a complete or close-to-complete α'-precipitation process in the simulation [60], which is not granted in the experiment. In particular, it has been shown in [64] that the SRO parameter which is measured experimentally is in fact the average over the whole sample of the SRO, which is actually negative in α and positive in and α'. The tendency to grow after reaching a minimum and the eventual change of sign do not reflect, therefore, a loss of order and the appearance of a purely random solute distribution, but only the average compensation of the negative value of the α phase, due to the segregation of Cr-rich α'. As a consequence, the results of both simulations and experiments become extremely sensitive to the actual advancement of the segregation process and to the actual microstructure, in terms of size and density of precipitates, and even simulation box size. Also experimentally important differences are found depending on the actual annealing or irradiation time [64]. Thus, it can be stated that all three models, even without explicitly including a magnetic component in terms of spin dynamics, do catch in a reliable way the effect, of magnetic origin, of the sign-inversion of the mixing enthalpy on the SRO in the Fe-rich region at temperature of practical interest, thereby proving their capability of describing the Fe–Cr alloy in the ferromagnetic region of the phase diagram.

4.2. The effect of low-energy states on the phase diagram

The possible ground states according to the BCC-99 polyhedron have been calculated for the three cohesive models and plotted in Fig. 8. For concentrations up to 30 at.% Cr, the formation energies of the ordered structures with the three models are very similar, with a few slightly negative values, due to the negative heat of mixing. Note, however, that, since structures with a concentration less than 10% were deliberately not explored and plotted, it would be premature to call these structures ground states, since lower energy structures under 10% may occur. For the middle range of concentrations, 30–70%, the formation energies for the 2BM and CE are significantly more spread out than for the CDM case. An important observation is that the formation energies in that concentration range are never lower than 60 meV for the CDM case, while at 50% Cr for CE and 2BM some are as low as 8 meV and −8 meV, respectively, the latter being clearly a ground state of the system. As a general statement, the formation energies of structures in the intermediate concentration region are significantly lower for CE and 2BM than for CDM. Above 70% Cr, the formation energies for CE and CDM become similar, while the 2BM provides significantly lower values that can also be negative near 90% Cr, due to the negative heat of mixing in the Cr-rich region in this case.

This short discussion regarding the low-energy states rationalizes the phase diagrams presented in Fig. 9. These were calculated using the ATAT package and implicitly account for the configurational entropy, beyond the RSM, i.e. allowing for the existence of ordered or partially ordered low-energy states. These calculations show that the RSM results can be misleading. Both 2BM and CE dramatically drop their T_{Crit} from about 2700 and 3400 K, respectively to a common value of about 1500 K, while T_{Crit} for CDM stays about the same. We interpret this as a clear consequence of the fact that, while many low-energy structures are predicted by 2BM and CE, hardly any is predicted by CDM. Note that the lack of closure of the MG in the figure stems only from numerical issues, that cause the algorithm to become very slow for intermediate concentrations, as a consequence of sudden slope changes; therefore the runs were interrupted after a clear tendency could be assured. Also note that the low solubility in the Fe-rich zone of the CDM is an artefact of the method, due to the cluster expansion fit in the ATAT package, where structures below 10% and above 90% are disregarded, so that negative values (which would ensure a large solubility at low temperature) could not be fitted in this specific case (better results could be obtained with the 2BM, possibly because of the lower maximum in the mixing enthalpy). This does not question, however, the validity of the calculation for other concentrations, particularly concerning the closure of the MG. Finally, note that in the case of the 2BM phase diagram for simplicity the

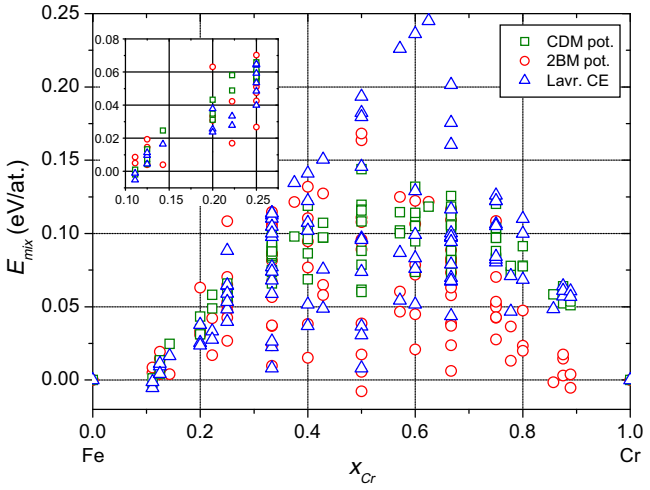

Fig. 8. The heat of formation for the BCC-99 structures calculated using the different cohesive models.

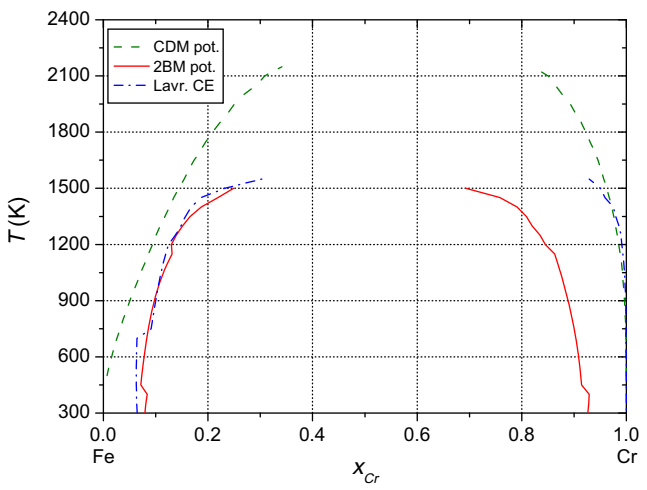

Fig. 9. The phase diagram according to the three cohesive models taking into account full configurational entropy.

intermetallic at 50% (ground state) was neglected. This choice is not expected to impact the results regarding T_{Crit}, but including this 'fake' intermetallic phase would certainly complicate the construction of the complete phase diagram, by introducing additional phase stability fields.

In summary, the large drop in T_{Crit} for the 2BM and CE is the consequence of the low-energy structures at intermediate concentrations, while the negligible drop in T_{Crit} for CDM is explained by the lack of them. This discussion illustrates the importance that low-energy structures may have on the phase diagram and of keeping them under control when fitting a semi-empirical cohesive model.

4.3. The effect of vibrational entropy on the phase diagram

The methodology to estimate the excess vibrational free energy outlined in Section 3.3 was applied with the 2BM and CDM potentials (not with the CE, since it is a rigid-lattice model). The results using the MJS and MD approaches are plotted together with experimental data [65] in Figs. 10 and 11 for 2BM and CDM, respectively. For the 2BM, the results for MJS and MD are quite similar, although the contributions estimated by MJS are slightly larger than by MD. This indicates an almost linear scaling of the MD results with temperature, suggesting little or no anharmonic behaviour due to the cohesive model. For the CDM, the results for MJS and MD are completely different, both qualitatively and quantitatively. The MD results suggest a saturation effect with temperature, showing that CDM introduces anharmonic behaviour in the system, making the results obtained by MJS unreliable (harmonic model). As a peculiarity of the cohesive model, the vibrational free energy changes sign with concentration and is positive in the Fe-rich region. This observation seems compatible with indirect calculations of the vibrational free energy for the same cohesive model reported in [41]. The apparent disagreement with indirect calculations performed with the same cohesive model in [8,66] is due, as explained in [41], to an incorrect evaluation of the free energy in those previous papers. When compared to experimental data [65] (500 K curve derived from 300 K data and 1500 K curve derived from high temperature limit, respectively), the 2BM seems to overestimate the vibrational contribution by about a factor 1.5. On the contrary the CDM largely underestimates the same contribution, by predicting a value that is a factor 6 smaller, and even opposite in sign, as compared to experiment in the Fe-rich region. It should be emphasised, at any rate, that in neither case was the vibrational entropy used for the fitting or verification of these potentials, therefore these results, whatever their quality, are totally fortuitous.

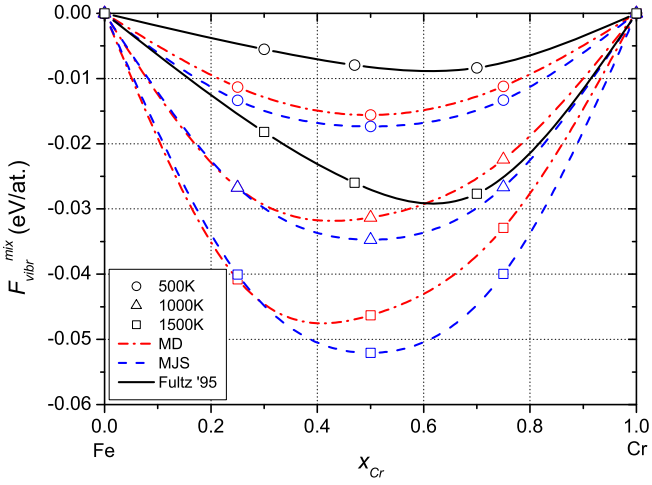

Fig. 10. The excess vibrational free energy evaluated with different methods using the 2BM interatomic potential.

The effect of the vibrational entropy on the MG is shown in Fig. 12. Here the phase diagram for the 2BM is obtained from a temperature dependent cluster expansion, fed to ATAT, so as to incorporate not only the configurational entropy, but also the vibrational one, according to the calculations shown in Fig. 10. The phase diagram for CDM, on the other hand, is taken from [41] and was obtained applying a full thermodynamic integration [40], thereby implicitly taking the vibrational entropy into account, though having modified the initial samples to include also short-range order effects in the Fe-rich region. The latter method is considered more reliable in the CDM case due to the anharmonic behaviour of the model. On the other hand, the thermodynamic integration method cannot account for low-energy states in the intermediate range concentrations, but, as discussed above, such states are absent in the case of the CDM cohesive model.

For the 2BM, the inclusion of the vibrational entropy makes T_{Crit} drop further, to about 1000 K, in close agreement with the Calphad

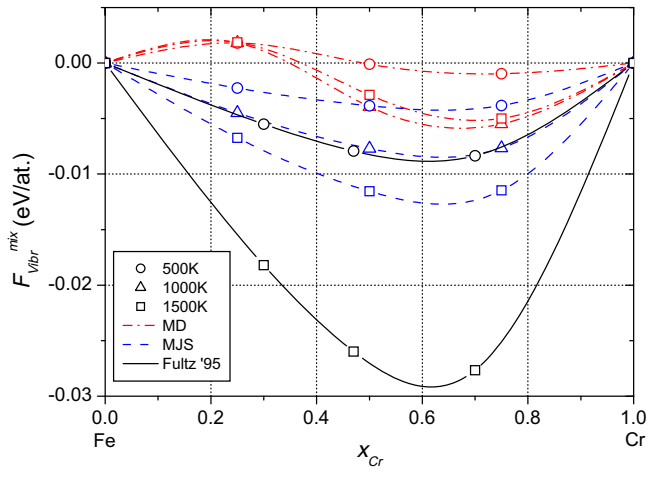

Fig. 11. The excess vibrational free energy evaluated with different methods using the CDM interatomic potential.

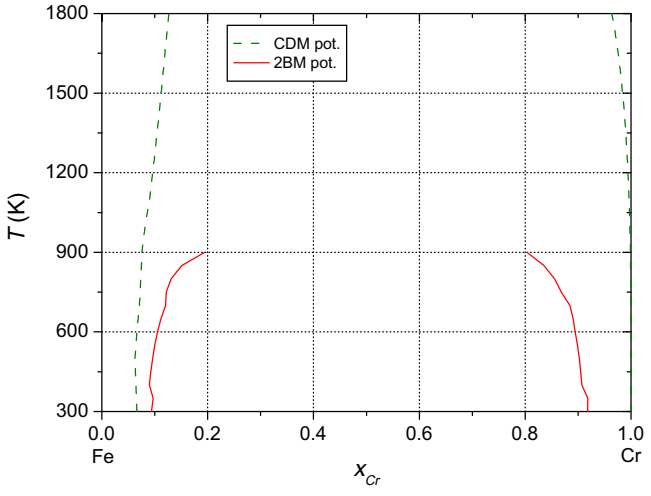

Fig. 12. The phase diagram according to the interatomic potentials taking into account configurational and vibrational entropy.

value of ~900 K for the metastable MG (see Fig. 1). Note that in Ref. [29] it was already shown that, by allowing in the CE for the vibrational entropy effect, based on an interpolation of the experimental measurements from [65], T_{Crit} also dropped to a value of the same order. In the CDM case, however, which provides almost negligible vibrational entropy, the phase boundaries are almost identical to those obtained using the RSM approach (see Fig. 4). This discussion illustrates the importance that the vibrational entropy can have on the MG and of correctly allowing for it when developing a cohesive model.

5. Concluding remarks

The thermodynamic properties of three different, non-magnetic, semi-empirical cohesive models describing the Fe–Cr alloy, namely two interatomic potentials (2BM [31] and CDM [30]) and a cluster expansion [29], have been compared and evaluated on the same footing. Despite apparent differences, 2BM and CDM are equivalent approaches, although no one-to-one relationship exists (Appendix A); the CE is, on the other hand, an inherently different type of model, of use only in a rigid-lattice approximation. All three models, notwithstanding the different reference data to which they were fitted, the different underlying fitting strategy and the different inherent features, succeed in their main original purpose, which was the reproduction of the mixing enthalpy sign-change and short-range order inversion in the Fe-rich region of the Fe–Cr alloy, at least up to a temperature of ~700 K. While CDM and CE were strictly fitted to DFT mixing enthalpy data in the whole range of composition, for the 2BM a mixed fitting approach was used, deliberately adopting a symmetric mixing enthalpy curve, with a negative part in the Cr-rich region, too, not supported by DFT data. This choice, though probably physically unjustified, allows the composition of the α'-phase to be correctly predicted at temperatures of technological interest by the 2BM, something that both CDM and CE fail to do. In addition, this model provides non-negligible vibrational entropy, in fair agreement with experimental measurements. On the other hand, this model exhibits a number of low-energy ordered structures, not necessarily observed in reality, including a 'fake' ground state at ~50% Cr. When all effects are allowed for, the T_{Crit} where the α–α' miscibility gap closes is found, for the 2BM cohesive model, to be around 1000 K, which is reasonably close to the experimental T_{Crit} of ~900 K, as reflected in the Calphad phase diagram. The CE from [29] also exhibits low-energy structures, but none of them is a ground state. However, because of the inherently rigid-lattice nature of this cohesive model, no vibrational entropy is implicitly provided by it: the latter must be estimated from experimental measurements, in order to be allowed for. T_{Crit} is found to be around 1500 K for this model, although including the experimentally measured contribution would lower this value to about 1000 K, too [29]. The CDM interatomic potential does not show low-energy states and provides a negligible contribution of vibrational entropy, thereby making a simple regular solution approach adequate to evaluate the corresponding phase diagram. Although at temperatures of technological interest it is basically equivalent to the other two cohesive models, its miscibility gap does not close in the solid phase.

From a more general point of view, this study has shown the impact that low-energy structures and vibrational entropy can have on the phase diagram, making it clear that the latter is not only dictated by the mixing enthalpy, although the concentration dependence of the mixing enthalpy curve (at 0 K) clearly has an important role. Thus, at least three 'ingredients' should be, in general terms, included and kept under control, when producing a semi-empirical cohesive model for an alloy, namely mixing enthalpy curve (at 0 K), low-energy states and vibrational entropy.

Of course, in the case of the presently studied alloy, the effect of magnetism on both enthalpy and entropy is expected to play a role, as suggested e.g. in [28]. A proper identification of the relative importance of this further 'ingredient', as compared to the other ones, could not be addressed here, because the presently available models specific for Fe–Cr do not include in any explicit way spins and their dynamics. We can therefore only speculate about this point. It seems reasonable to expect that magnetic entropy will have an impact on the thermodynamic properties, e.g. on the shape of the MG, mainly at high temperature, when approaching the Curie temperature, T_C. It is also in this range where magnetism will have an effect in determining the stability of low-energy structures and, in general, the mixing enthalpy. Then, above T_C, a second order magnetic transition to the paramagnetic state occurs, which of course cannot be allowed for by models not including spins. Nonetheless, we have clearly shown that, even without explicitly including magnetism, the models here analysed do succeed in catching phenomenologically its main effects on the thermodynamic behaviour of Fe–Cr alloys, certainly up to 700 K, a temperature up to which they can be reliably used. Above this temperature, too, they perform reasonably well, particularly the 2BM. It can thus be stated that magnetism is only one more 'ingredient' to be allowed for, explicitly or implicitly, in a semi-empirical cohesive model. Even a model explicitly including spin dynamics will have to cope with a proper description of the mixing enthalpy, the low-energy structures and, above all, the vibrational entropy which, in the case of Fe–Cr, is clearly one of the main contributors to determining the phase diagram at high temperature.

Finally, this work has also enlightened some misconceptions about the thermodynamic performance of the different existing cohesive models for Fe–Cr, as well as about the methods used to evaluate them. In particular, it has evidenced the difficulty of getting a clear perception of the thermodynamic properties predicted by a given model, if only one method is used, since the assumptions made in setting up the method may not be suitable to allow for all effects of importance. In other words, depending on the used modelling tool, the same cohesive model may perform differently and provide different thermodynamic properties for the same system. This unfortunate fact clearly complicates the task of systematically evaluating the thermodynamic performance of available cohesive models and, conversely, the task of producing thermodynamically fully reliable models.

Acknowledgements

The research leading to these results has received partial funding from the European Atomic Energy Community's 7th Framework Programme (FP7/2007–2011), under Grant Agreement No. 212175 (GetMat project). These results also contribute to the European Fusion Programme coordinated by the EFDA Fusion Materials Topical Group. RCP wishes to acknowledge partial support from CONICET-PIP 5062 and UNSAM c032.

Appendix A. 2BM vs. CDM

In this appendix the 2BM and CDM formalisms are compared. The total energy within CDM can be written as

$$E_{CDM} = E_{EAM} + \frac{1}{2}\sum_{i,j}(h(x_{ij}) - 1)\,V_{AB}(R_{ij})\,(1 - \delta_{t_i t_j}), \tag{A1}$$

where t_i is the atom-type occupying site i. Within 2BM the total energy is in turn

$$E_{2BM} = E_{EAM} + \sum_i F^s_{t_i}. \tag{A2}$$

The latter term of the above equation can easily be recasted as

$$\begin{aligned}\sum_i F^s_{t_i} &= \sum_i \frac{F^s_{t_i}}{\rho^s_i}\rho^s_i \\ &= \sum_{\substack{i,j \\ (i\neq j)}} \frac{F^s_{t_i}}{\rho^s_i}\varphi^s_{t_i t_j}(R_{ij}) \\ &= \frac{1}{2}\sum_{\substack{i,j \\ (i\neq j)}} \left(\frac{F^s_{t_i}}{\rho^s_i}+\frac{F^s_{t_j}}{\rho^s_j}\right)\varphi^s_{t_i t_j}(R_{ij}) \\ &= \frac{1}{2}\sum_{i,j} \left(\frac{F^s_{t_i}}{\rho^s_i}+\frac{F^s_{t_j}}{\rho^s_j}\right)\varphi^s_{AB}(R_{ij})(1-\delta_{t_i t_j})\end{aligned} \tag{A3}$$

Identifying Eqs. (A1) and (A2) one finds the relationship between both formalisms

$$\left(\frac{F^s_{t_i}}{\rho^s_i}+\frac{F^s_{t_j}}{\rho^s_j}\right)\varphi^s_{\mathrm{AB}}(R_{ij}) = (h(x_{ij})-1)V_{\mathrm{AB}}(R_{ij}). \tag{A4}$$

The left factors in both sides of Eq. (A4) are functions of a variable depending on the local concentration, while the right factor is a function depending on the distance between two atoms. Heuristically, one can further identify

$$\frac{F^s_A[\rho^s_A(x)]}{\rho^s_A(x)}+\frac{F^s_B[\rho^s_B(x)]}{\rho^s_B(x)} = 1-h(x) \tag{A5}$$

$$\varphi^s_{\mathrm{AB}}(R) = -V_{\mathrm{AB}}(R). \tag{A6}$$

Formally, there is no one-to-one relationship between $\rho^s_{t_i}$ and x_{AB} since both quantities depend on the local concentration, which can be different from the global concentration x. Therefore, it is not possible to make a 2BM potential which is an exact replica of a CDM potential. However, in terms of mixing enthalpy, Eqs. (A5) and (A6) could be used to find a match between the potentials. Practically, Eqs. (A5) and (A6) suggest that choosing a non-monotonic s-density within the 2BM formalism is equivalent to the development of a CDM potential.

References

[1] L.K. Mansur, A.F. Rowcliffe, R.K. Nanstad, S.J. Zinkle, W.R. Corwin, R.E. Stoller, J. Nucl. Mater. 329–333 (2004) 166.
[2] M.L. Jenkins, C.A. English, B.L. Eyre, Philos. Mag. A 38 (1978) 97.
[3] E.A. Little, D.A. Stow, J. Nucl. Mater. 87 (1979) 25.
[4] E.A. Little, R. Bullough, M.H. Wood, Proc. R. Soc. London A 372 (1980) 565.
[5] F.A. Garner, M.B. Toloczko, B.H. Sencer, J. Nucl. Mater. 276 (2000) 123.
[6] S.J. Zinkle, Phys. Plasmas 12 (2005) 058101.
[7] L. Malerba, D. Terentyev, G. Bonny, A.V. Barashev, C. Bjorkas, N. Juslin, K. Nordlund, C. Domain, P. Olsson, N. Sandberg, J. Wallenius, J. ASTM International 4 (2007) JAI100692.
[8] L. Malerba, A. Caro, J. Wallenius, J. Nucl. Mater. 382 (2008) 112.
[9] N. Saunders, A.P. Miodownik, CALPHAD Calculation of Phase Diagrams, A Comprehensive Guide, Pergamon, 1998.
[10] J.-O. Andersson, B. Sundman, CALPHAD 11 (1987) 83.
[11] T. De Nys, P.M. Gielen, Metall. Trans. 2 (1971) 1423.
[12] H. Kuwano, Trans. Japan Inst. Met. 26 (1985) 473.
[13] S.M. Dubiel, G. Inden, Z. Metallkde 78 (1987) 544.
[14] I. Mirebeau, M. Henion, G. Parette, Phys. Rev. Lett. 53 (1984) 687.
[15] N.P. Filippova, V.A. Shabashov, A.L. Nikolaev, Phys. Met. Metall. 90 (2000) 145.
[16] P. Olsson, I.A. Abrikosov, L. Vitos, J. Wallenius, J. Nucl. Mater. 321 (2003) 84.
[17] A.A. Mirzoev, M.M. Yalalov, D.A. Mirzaev, Phys. Met. Metall. 97 (2004) 336.
[18] T.P.C. Klaver, R. Drautz, M.W. Finnis, Phys. Rev. B 74 (2006) 094435.
[19] P. Olsson, I.A. Abrikosov, J. Wallenius, Phys. Rev. B 73 (2006) 104416.
[20] D. Nguyen-Mahn, M.Yu. Lavrentiev, S.L. Dudarev, J. Comput. Aided Mater. Des. 14 (2007) 159.
[21] P. Olsson, C. Domain, J. Wallenius, Phys. Rev. B 75 (2007) 014110.
[22] P. Erhart, B. Sadigh, A. Caro, Appl. Phys. Lett. 92 (2008) 141904.
[23] R. Hafner, D. Spišák, R. Lorenz, J. Hafner, J. Phys.: Condens. Matter 13 (2001) L239.
[24] J. Wallenius, P. Olsson, C. Lagerstedt, N. Sandberg, R. Chalarova, V. Pontikis, Phys. Rev. B 69 (2004) 094103.
[25] A. Caro, P.E.A. Turchi, M. Caro, E.M. Lopasso, J. Nucl. Mater. 336 (2005) 233.
[26] M.S. Daw, M.I. Baskes, Phys. Rev. B 29 (1984) 6443.
[27] M.W. Finnis, J.E. Sinclair, Phil. Mag. A 50 (1984) 45.
[28] G.J. Ackland, Phys. Rev. Lett. 97 (2005) 015502.
[29] M.Y. Lavrentiev, R. Drautz, D. Nguyen-Mahn, T.P.C. Klaver, S.L. Dudarev, Phys. Rev. B 75 (2007) 14208.
[30] A. Caro, D.A. Crowson, M. Caro, Phys. Rev. Lett. 95 (2005) 75702.
[31] (a) P. Olsson, J. Wallenius, C. Domain, K. Nordlund, L. Malerba, Phys. Rev. B 72 (2005) 214119;
(b) P. Olsson, J. Wallenius, C. Domain, K. Nordlund, L. Malerba, Phys. Rev. B 74 (2006) 1(E).
[32] J.M. Sanchez, F. Ducastelle, D. Gratias, Physica A 128 (1984) 334.
[33] G.J. Ackland, M.I. Mendelev, D.J. Srlolovitz, S. Han, A.V. Barashev, J. Phys.: Condens. Matter 16 (2004) 1.
[34] M.I. Mendelev, S.W. Han, D.J. Srolovitz, G.J. Ackland, D.Y. Sun, M. Asta Phil. Mag. A 83 (2003) 3977.
[35] O. Redlich, A.T. Kister, Indust. Eng. Chem. 40 (1948) 345.
[36] G.J. Ackland, S.K. Reed, Phys. Rev. B 67 (2003) 174108.
[37] D.A. Porter, K.E. Easterling, Phase Transformations in Metals and Alloys, 2nd Ed., CRC Press, 1992.
[38] A. van de Walle, G. Ceder, J. Phase Equilibria 23 (2002) 348.
[39] A. van de Walle, M. Asta, Modelling Simul. Mater. Sci. Eng. 10 (2002) 521.
[40] E.M. Lopasso, M. Caro, A. Caro, P.E.A. Turchi, Phys. Rev. B 68 (2003) 214205.
[41] G. Bonny, P. Erhart, A. Caro, R.C. Pasianot, L. Malerba, M. de Caro, The influence of short range order on Fe–Cr thermodynamics, Modelling Simul. Mater. Sci. Eng., accepted for publication.
[42] D. Frenkel, B. Smit, Understanding Molecular Simulation – From Algorithms to Applications, Academic Press, London, 1996.
[43] V.L. Moruzzi, J.F. Janak, K. Schwartz, Phys. Rev. B 37 (1978) 790.
[44] L.G. Ferreira, S.-H. Wei, A. Zunger, Int. J. Supercomput. 5 (1991) 34.
[45] F. Ducastelle, Order and Phase Stability in Alloys, Elsevier Science Publisher B.B., North Holland, 1991.
[46] G. Inden, W. Pitsch, in: R.W. Cahn, P. Haasen, C.J. Kramers (Eds.), Phase Transformations in Materials, Materials Science and Technology, vol. 5, John Wiley, Weinheim, 1991, p. 497 (Chapter 9).
[47] A. Finel, PhD thesis, Université Pierre et Marie Curie, Paris, 1987.
[48] R.C. Pasianot, L. Malerba, J. Nucl. Mater. 360 (2007) 118.
[49] P.E. Blöchl, Phys. Rev. B 50 (1994) 17953.
[50] G. Kresse, J. Hafner, Phys. Rev. B 47 (1993) 558.
[51] G. Kresse, J. Furthmüller, Phys. Rev. B 54 (1996) 11169.
[52] G. Kresse, J. Furthmüller, Comput. Mater. Sci. 6 (1996) 15.
[53] G. Kresse, D. Joubert, Phys. Rev. B 59 (1999) 1758.
[54] A. Zunger, S.H. Wei, L.G. Ferreira, J.E. Bernard, Phys. Rev. Lett. 65 (1990) 353.
[55] S.H. Vosko, L. Wilk, M. Nusair, Can. J. Phys. 58 (1980) 1200.
[56] W.A. Dench, Trans. Faraday Soc. 59 (1962) 1279.
[57] S.S. Brenner, M.K. Miller, W.A. Soffa, Scripta Metall. 16 (1982) 831.
[58] M.H. Mathon, Y. De Carlan, G. Geoffroy, X. Averty, C.H. de Novion, A. Alamo, in: Effects of radiation on materials, in: S.T. Rosinski, M.L. Grossbeck, T.R. Allen, A.S. Kumar (Eds.), 20th International Symposium, ASTM STP 1405, American Society for Testing and Materials, West Conshohocken, PA, 2001, p. 674.
[59] M.H. Mathon, Y. de Carlan, G. Geofroy, X. Averty, A. Alamo, C.H. de Novion, J. Nucl. Mater. 312 (2003) 236.
[60] G. Bonny, D. Terentyev, L. Malerba, Comput. Mater. Sci. 42 (2008) 107.
[61] R. Hafner, D. Spišák, R. Lorenz, J. Hafner, Phys. Rev. B 65 (2002) 184432;
R. Hafner, D. Spišák, R. Lorenz, J. Hafner, J. Phys.: Condens. Matter. 14 (2002) 2119.
[62] S. Cottenier, B. De Vries, J. Meersschaut, M. Rots, J. Phys.: Condens. Matter. 14 (2002) 3275.
[63] L. Malerba, On the thermodynamic validation of two-band model potentials for FeCr, SCK•CEN External Report ER-16, June 2006.
[64] P. Erhart, A. Caro, M. Serrano de Caro, B. Sadigh, Phys. Rev. B 77 (2008) 134206.
[65] B. Fultz, L. Anthony, J.L. Robertson, R.M. Nicklow, S. Spooner, M. Mostoller, Phys. Rev. B 52 (1995) 3280.
[66] A. Caro, M. Caro, E.M. Lopasso, D.A. Crowson, Appl. Phys. Lett. 89 (2006) 121902.